HHS Public Access

Author manuscript

Cancer Res. Author manuscript; available in PMC 2017 June 15.

Published in final edited form as:

Cancer Res. 2016 June 15; 76(12): 3451–3462. doi:10.1158/0008-5472.CAN-16-0270.

Label-Free Neurosurgical Pathology with Stimulated Raman Imaging

Fa-Ke Lu[1,2], **David Calligaris**[1], **Olutayo I. Olubiyi**[1], **Isaiah Norton**[1], **Wenlong Yang**[2], **Sandro Santagata**[3,4,*], **X. Sunney Xie**[2,*], **Alexandra J. Golby**[1,5,*], and **Nathalie Y. R. Agar**[1,4,5,**]

[1]Department of Neurosurgery, Brigham and Women's Hospital, Harvard Medical School, Boston, Massachusetts, USA.

[2]Department of Chemistry and Chemical Biology, Harvard University, Cambridge, Massachusetts, USA.

[3]Department of Pathology, Brigham and Women's Hospital, Harvard Medical School, Boston, Massachusetts, USA.

[4]Department of Cancer Biology, Dana-Farber Cancer Institute, Boston, Massachusetts, USA.

[5]Department of Radiology, Brigham and Women's Hospital, Harvard Medical School, Boston, Massachusetts, USA.

Abstract

The goal of brain tumor surgery is to maximize tumor removal without injuring critical brain structures. Achieving this goal is challenging since it can be difficult to distinguish tumor from non-tumor tissue. While standard histopathology provides information that could assist tumor delineation, it cannot be performed iteratively during surgery as freezing, sectioning, and staining of the tissue require too much time. Stimulated Raman scattering (SRS) microscopy is a powerful label-free chemical imaging technology that enables rapid mapping of lipids and proteins within a fresh specimen. This information can be rendered into pathology-like images. Although this approach has been used to assess the density of glioma cells in murine orthotopic xenografts models and human brain tumors, tissue heterogeneity in clinical brain tumors has not yet been fully evaluated with SRS imaging. Here we profile 41 specimens resected from 12 patients with a range of brain tumors. By evaluating large-scale stimulated Raman imaging data and correlating this data with current clinical gold standard of histopathology for 4,422 fields of view, we capture many essential diagnostic hallmarks for glioma classification. Notably, in fresh tumor samples we observe additional features, not seen by conventional methods, including extensive lipid droplets within glioma cells, collagen deposition in gliosarcoma, and irregularity and disruption of myelinated fibers in areas infiltrated by oligodendroglioma cells. This data is freely available in a public resource to foster diagnostic training and to permit additional interrogation. Our work

[*]To whom correspondence should be addressed. ssantagata@bics.bwh.harvard.edu, xie@chemistry.harvard.edu, agolby@bwh.harvard.edu. [**]Corresponding author for this manuscript: Nathalie Y.R. Agar, Department of Neurosurgery, Brigham and Women's Hospital, Harvard Medical School, 221 Longwood Avenue, BLI-137, Boston, Massachusetts 02115, Tel: 617.525.7374, Fax: 617.264.6316, Nathalie_Agar@dfci.harvard.edu.

Conflict of interest statement: X.S.X is a cofounder of Invenio Imaging, Inc., USA. N.Y.A. and S.S. are cofounders of BayesianDx.

establishes the methodology and provides a significant collection of reference images for label-free neurosurgical pathology.

Keywords

stimulated Raman scattering microscopy; label-free neurosurgical pathology; cancer; brain tumor; glioma

Introduction

Surgery remains the most important treatment of brain tumors. Gross total resection of tumors is associated with longer survival time and improved neurological function (1). On the other hand, surgical injury of the eloquent cortical areas may produce severe neurological deficits (2). Preoperative magnetic resonance images coregistered to the patient via neuronavigation systems is commonly used to guide surgery intraoperatively. However, resection of tumor tissue causes the surrounding brain to shift, which increasingly reduces spatial accuracy (3). Moreover, while MRI is the gold standard for delineating tumor boundaries, tumor cells invariably extend beyond the MRI signal abnormality (4).

The review of hematoxylin and eosin (H&E) stained cryosections is often used during surgery to provide a preliminary diagnosis. However, it is not practical to use frozen section pathology to actively guide and optimize the extent of tumor resection because of inherent limitations of this approach. Freezing tissues generates substantial artifacts, which can limit diagnostic evaluation. Moreover, the microscopic review of frozen sections is labor-intensive, time-consuming (~30 min), and costly (5). While formalin fixation and paraffin embedding tissue provides high quality material for rendering a final pathologic diagnosis, the processing steps involve the use of xylene, an organic solvent that removes lipids. As a result, capturing and assessing lipid-related diagnostic information is not possible.

Fluorescence imaging has been developed and tested as a tool to help guide the resection of high-grade gliomas (6,7). Despite encouraging results, this approach is not always reliable for identifying tumor tissue at the interface with normal tissue (8). This limitation is particularly problematic for low-grade gliomas (9). Other techniques such as Raman spectroscopy (10-12) and optical coherence tomography (13,14) have also been used to characterize brain tumor tissues. Such techniques rely on statistical analysis and classification, which can be excessively complex for practical applications. A microscopic imaging approach that could provide histopathological information directly from the surgically removed fresh tissue, or from *in situ* tissues, could allow for the evaluation of features that are assessed during traditional histopathological diagnosis. Such a capability could enable the identification of cancer cells in the operating room in multiple iterative tissue sampling steps.

The phenomenon of stimulated Raman scattering (SRS) was first discovered in 1962 (15). SRS spectroscopy and microscopy were demonstrated in 1977 and 2007, respectively (16,17). In 2008, the Xie group reported high-speed, high-sensitivity single frequency SRS microscopic imaging with megahertz modulation of a picosecond laser and lock-in detection

of the modulation transfer to the other picosecond laser (18). Recently, more technical developments have enable SRS microscopy as a powerful tool for rapid label-free biochemical imaging of cells and tissues with submicron resolution (19-26). In modern SRS microscopy, two laser beams at different wavelengths are used to excite a sample. These beams are denoted as pump and Stokes beams at frequencies ω_p and ω_s, respectively. When tuning the frequency difference (ω_p-ω_s) to the frequency of a particular Raman-active molecular vibrational mode, a SRS signal is generated due to a nonlinear process similar to stimulated emission with dramatic amplification of the ultra-weak Raman signals by a few orders of magnitude (Fig. 1A and B). In contrast, when the frequency difference does not match any vibrational resonance, SRS does not occur, providing high molecular selectivity and specificity without a nonresonant background (27,28).

SRS microscopy, and another similar modality coherent anti-Stokes Raman scattering (CARS), have been used for detecting brain tumor cells in both mouse xenografts and human resection tissues (29-32). The label-free mapping of protein and lipid with SRS can be used to generate pathology-like tissue images (33). Using SRS or CARS imaging, neoplastic glioma cells were identified based on both cellular morphology and the higher protein signals found in regions of densely packed cancer cells. However, brain tumor resection samples are often highly heterogeneous, and identification of tumor cells in such complex settings has not been fully investigated and validated. In addition, some quantitative classification approaches may be suboptimal in the context of complex tissues, which include pools of red blood cells, areas of apoptotic and necrotic cells, and reactive changes including gliosis. Furthermore, glioma cells infiltrate both white matter areas comprised of abundant myelin with strong a lipid signal and gray matter areas enriched in cell bodies with a low lipid signal. Thus, evaluating protein/lipid ratios without considering cytomorphology and tissue architecture may lead to inaccurate tissue characterization.

To establish label-free neurosurgical pathology with stimulated Raman imaging (SRI), it is important to evaluate large regions from tissue resection specimens, in a manner that is analogous to how pathologists scan and assess information from multiple broad fields of view during conventional histopathologic evaluations. In the present work, we acquired 4,422 fields of view (FOV; each ~350×350 μm) for 41 surgically removed brain specimens from 12 human subjects. Through comprehensive evaluation and correlation of these SRS images with H&E staining, we characterized and confirmed the ability of SRI to capture the fundamental diagnostic hallmarks traditionally used for the histopathologic classification of tumors as well as features that are not captured by conventional approaches.

Materials and Methods

Experimental design

We imaged both fresh and frozen human brain tumor tissue with stimulated Raman scattering (SRS) microscopy and thereafter stained the same frozen sections with H&E for validation. Working with a board certified neuropathologist (S.S.), all paired SRS and H&E images were pixel-to-pixel registered and side-by-side evaluated using 3D Slicer (a software platform for the analysis and visualization of medical images and for research in image guided therapy, www.slicer.org) (34). This study included 12 surgical cases. Informed

consent was obtained from each patient. The neurosurgeon (A.J.G.) and the neuropathologist (S.S.) were blinded to any information about SRS imaging during surgery and histological analysis. Clinical reports of the patients were accessible to certified personnel (O.I.O., S.S., A.J.G., and N.Y.A.) for data analysis.

Tissue preparation

All brain tissue samples were obtained from the Brigham and Women's Hospital and Dana-Farber Cancer Institute Neurooncology Program Biorepository collection, and analyzed under approved Institutional Review Board protocols. Samples were flash frozen in liquid nitrogen and stored at -80 degrees Celsius until sectioned at 12-μm thicknesses using a cryostat (Microm HM550, Thermo Scientific). Frozen sectioned slides were imaged with SRS microscopy and then were fixed for H&E staining. Fresh brain tissue samples were cut to thin slices at 1-mm thickness manually using a blade and then were sandwiched between a slide and coverglass for direct SRS imaging. Some pressure was applied to flatten the tissue.

Stimulated Raman scattering (SRS) microscopy

SRS imaging system is composed of an ultrafast laser source (picoEmerald, APE GmbH) and a modified laser-scanning confocal fluorescence microscope (FV300, Olympus). The picoEmerald combines a picosecond optical parametric oscillator (OPO) and its pump oscillator (picoTrain, High Q Laser) incorporated in a single housing. OPO supplies the tunable pump beam (720-990 nm, pulse width 5-6 ps), and a small portion of the oscillator output supplies the Stokes beam at 1064 nm (pulse width 7 ps) for SRS. The pump and Stokes beams are collinearly introduced into the microscope and are tightly focused onto the sample using water-immersion objectives. Imaging is realized by raster scanning the tightly focused laser beams across the sample. Frequency difference between the two beams determines the Raman shift to image. By tuning OPO wavelength, spectral/multicolor imaging can be achieved. The laser source can be completely remote controlled through RS-232 interface. A single field of view (FOV) is ~350 × 350 μm with objective 1 (XL PLAN N 25×, NA 1.05; Olympus) and is ~150 × 150 μm with objective 2 (UPlanApo IR 60×, NA 1.2; Olympus). Each FOV was acquired with 512 × 512 pixels in ~1 second. Tiling imaging is performed with an automated stage (MS2000, ASI). To realize high sensitive SRS imaging largely free from the laser noise, Stokes beam is modulated at ~10 MHz using an electro-optic modulator, and the modulation transferred to the pump beam (stimulated Raman loss) is detected using a homebuilt all-analog lock-in amplifier. A Si photodiode detector is used to convert the pump light to electrical signals. LabVIEW (National Instruments Corporation) programming integrates the whole system for automatic image acquisition. More details about the system were described previously (25).

Hematoxylin and eosin (H&E) staining

H&E staining was perform for each frozen sectioned slide after SRS imaging, using the following procedure: (1) fix the tissue section in 100% methanol for 2 min, (2) wash in deionized water for 10 sec, (3) stain in Hematoxylin solution (Harris modified) for 1.5 min, (4) wash in deionized water for 10 sec, (5) dip in bluing reagent (0.1% (v/v) ammonia water solution) for 1 sec, (6) wash in deionized water for 1 sec, (7) counterstain in Eosin Y for 8

sec, (8) wash and dehydrate in 100% ethanol for 10 sec, (9) wash and dehydrate again in 100% ethanol for 10 sec, (10) dip in xylene for 6 sec, and (11) dip in xylene again for 12 sec. Sections were then dried at room temperature and sealed with histological mounting medium and a coverglass. All reagents used were purchased from Sigma-Aldrich. H&E slides were imaged with a slide scanner (Axio Scan.Z1, Zeiss).

Luxol fast blue (LFB) staining

LFB staining of myelin sheath was performed for tissue sections adjacent to the sections used for SRS and H&E imaging to identify white matter of the brain tissue. The procedure used was as follows: (1) brain tissue section was fixed in 100% methanol for 2 min, (2) de-fatted by placing the slide directly in 1:1 (v/v) ethanol/chloroform for 2-3 hr, (3) rehydrated in 95% (v/v) ethanol for 5 min, (4) stain in 0.1% (w/v) LFB solution (American MasterTech, CA) for 2 hr in a water bath at 60 degrees Celsius, (5) rinsed in 95% (v/v) ethanol for 10 sec, (6) rinsed in deionized water, (7) differentiated in 0.05% (w/v) lithium carbonate solution for 30 sec (Sigma-Aldrich), (8) dehydrated in 70% (v/v) ethanol for 30 sec, (9) rinsed in deionized water for 10 sec, (10) dehydrated in 95% (v/v) ethanol for 5 min, (11) and in 100 ethanol twice (each 5 min), (12) followed by 100% xylene twice (each for 5 min). Sections were then dried at room temperature and sealed with histological mounting medium and a coverglass. LFB slides were imaged with a slide scanner (Axio Scan.Z1, Zeiss).

Image processing and data evaluation

As the field of view (FOV) of SRS imaging is brighter in the center than the periphery region due to limited chromatic aberration correction of the objective, to flatten each FOV, the image was multiplied by an adjustable 2D Gaussian profile with Matlab programming. The whole image of the tissue section was acquired with tiling scanning. Two-color SRS images of a single field of view was aligned using the registration plugin (SIFT) in Fiji (ImageJ), and all the sub-images (typically 100-400) for one section were stitched together using the Grid/Collection stitching plugin in Fiji. We defined that protein (blue) signal is equal to the SRS signal at 2940 cm^{-1} subtracted by half of the SRS signal at 2854 cm^{-1}, and defined lipid (green) signal is equal to the SRS signal at 2854 cm^{-1}. Cell density was estimated using the Fiji plugin Cell Counter for both SRS and H&E images. Cell density was defined as the number of cell nuclei per FOV. The correlation between the cell densities estimated from SRS and H&E was calculated using OriginPro. The computations were run on the Odyssey cluster supported by the FAS Division of Science, Research Computing Group at Harvard University. SRS and H&E images of the same frozen section were pixel-to-pixel registered using mainly the following 3D Slicer modules: Volumes, Transforms, Resample Image (BRAINS), and Crop Volume (www.slicer.org). All SRS and H&E images were evaluated side-by-side in 3D Slicer together with a board-certificated neuropathologist (S.S.).

Results

Multicolor label-free tissue imaging with SRS

We acquired spatially-registered high spectral resolution data (~5 cm^{-1}) from a range of tissues including normal human brain and brain tumors using a picosecond laser source that

permits imaging of single Raman shifts (Fig. 1B). We tuned the pump beam frequency to acquire the carbon-hydrogen (CH) stretching vibrational band (2800-3050 cm^{-1}) and plotted this data to generate SRS images. We plotted the SRS spectra of white matter, gray matter, tumor, and necrosis in human surgical resection tissues (Fig. 1C). These areas were selected by evaluating serial H&E stained sections. The SRS spectra confirmed distinct spectral features resulting from their different chemical compositions.

Previous studies have demonstrated that SRS imaging of tissue at ~2854 cm^{-1} mainly maps the distribution of lipids with high vibrational contrast, and imaging at ~2940 cm^{-1} maps the distribution of both protein and lipid (35). We used a simple linear unmixing process to extract and retrieve information about the distribution of proteins from the signal generated by the protein/lipid Raman shift. We assigned lipid signals to the green channel and protein signals to the blue channel (Fig. 1B). In these two-color images, red blood cells appear cyan colored (greenish-blue) because hemoglobin yields strong non-Raman two-photon two-color absorption signals in both channels (36). We also tuned to the third Raman-silent frequency at 2800 cm^{-1} to image hemoglobin in a separate channel and assigned that signal a magenta color. Having tuned our SRS system to these parameters, we proceeded to image a panel of brain tissues that either had been frozen and cryosectioned or that had been freshly harvested (Supplementary Table S1).

Rapid identification of white and gray matter

Myelin sheaths are a lipid-rich cellular structure that surround axons and play important roles in axonal insulation, action-potential propagation, and trophic support (37). The lipids comprising myelin yielded strong SRS signals (colored green). Thus, white matter regions of the brain, which have abundant myelin lipids, appeared green in our SRS images and gray matter regions, which contain more cell bodies, appeared blue due to their higher relative protein composition. These striking patterns can be seen in Fig. 1D that shows an SRS image of fresh (i.e. unfrozen) brain tissue at the gray and white matter junction from a portion of brain tissue removed from an epilepsy patient with focal cortical dysplasia (case 43). The margin between white and gray matter was clearly identified with submicron spatial resolution (~400-500 nm). Single myelinated axon fibers were visualized and traced in the transition zone from white matter to gray matter (Fig. 1D, right). Blood vessels appeared blue due to the high protein content of both the cells of the vessel walls, and the blood contents in the vessel lumen. (Fig. 1D, one example marked by a “V”).

To further evaluate the contrasts, we imaged sections from frozen autopsy brain samples with SRS that contained both normal gray and white matter (Fig. 1E, left, case A1). We then stained the identical slices with H&E (Fig. 1E, middle) and a serial section with Luxol Fast Blue (LFB, Fig. 1E, right) to permit direct comparisons between SRS images and images acquired using standard microscopy techniques. We observed the striking contrast between gray and white matter in these frozen sections (Fig. 1E, left) and also identified single myelinated axon fibers (Fig. 1F). The SRS images acquired from frozen tissues contained artifacts that were similar to those typically observed in H&E stained sections. These artifacts included disruption of the myelin signal along the length of the axon fibers as well

as distortion and interspersed cracks (Fig. 1F). Similar artifacts are not present in SRS images of fresh, unfrozen tissues.

We next imaged an additional piece of frozen brain tissue, scanning a region 7 mm in length. We quantified the intensity profile of the SRS signals and demonstrated that the lipid signal was ~2-fold stronger in the white matter (left) than in the gray matter (right) (Fig. 1G). In contrast, the protein signal in the gray matter was only slightly higher than the protein signal in the white matter. SRS and H&E stained images showed clear correlation at the sub-cellular level. However, the visual differences between gray and white matter areas in the images from H&E stained sections were less obvious than the marked molecular differences captured by SRS imaging. Our results open new possibilities for using high resolution SRS imaging of myelin and various lipids to characterize both healthy tissues and those characteristic of focal cortical dysplasias, and adult and pediatric demyelinating diseases (38).

We then applied our SRS imaging approach to characterize a range of tissue types obtained during brain tumor resections. These tissue samples included tissues from resections of gliomas of different WHO grades such as WHO grade II oligodendroglioma, WHO grade III anaplastic oligodendroglioma and anaplastic oligoastrocytoma, and WHO grade IV glioblastoma including one case of gliosarcoma (Supplementary Table S1). Figure 2A shows the SRS image of an entire frozen biopsy specimen taken during the surgical resection of an anaplastic oligodendroglioma (WHO grade III; case 15, specimen B2,). A large region of the specimen (Fig. 2A, left, upper part of the SRS image) generated strong lipid signals (green) due to an abundance of myelinated axon fibers while another large region of the specimen (Fig. 2A, left, lower bottom part of the SRS image) generated strong protein signals (blue). The presence of infiltrating glioma cells in both of these regions was observed in the SRS image, which was validated by review of the H&E staining (Fig. 2A, right). Again, the boundary between the gray matter and the white matter was clearer in the SRS images than in images obtained from H&E stained sections (Fig. 2) in which lipids have been largely removed during sample processing. Identification of the nuclei from individual cells, however, is robust in both SRS and H&E stained sections (Fig. 2B). Regions of micro-hemorrhages that occur during the biopsy procedure were also well visualized in both SRS and H&E-stained images (Fig. 2A). In the SRS images, red blood cells appear cyan colored due to the non-Raman two-photon two-color absorption by these cells (Fig 2A, left, two regions of micro-hemorrhage marked by V).

Visualization and quantification of (hyper)cellularity

The World Health Organization (WHO) classification scheme is widely used by neuropathologists for classifying and grading glial brain tumors (39). Increased cellularity (hypercellularity) is a hallmark feature of malignant brain tumors. Figure 3A shows paired SRS and H&E images of a whole specimen from a glioblastoma surgical resection (specimen #3, case 22, GBM). Hypercellularity was readily detected in SRS images, which capture large round shapes of tumor cell nuclei, densely packed against one another (Fig. 3A and B). There was high cell-to-cell correlation between SRS and H&E images. This correlation was also very high in images from non-neoplastic brain tissue resected during

surgery (epilepsy, specimen A1, case 42), even in the presence of low cellular density (Fig. 3C and D).

We next quantified cell density from both SRS and H&E images. Considering the complexity of tissue heterogeneity, we performed manual cell counts (see Materials and Methods). Representative fields of view for cell counting are shown in Fig. 3B and D (left). We found very high correlation ($R^2 = 0.99$) between the cell density (cell numbers per FOV, 350 μm × μm) estimated from SRS and H&E images (Fig. 3E). We also noted that the cell density estimated from the SRS images was consistently ~20% lower than that from the H&E images (Fig. 3F). This discrepancy may be because the label-free cell nuclei contrasts from SRS were weaker than that from H&E and some cell nuclei were not seen, especially in the region with strong lipid signals. Future technical improvements are necessary to enhance the contrast for visualization and quantification of cell nuclei. We plotted the estimated cell density of different tissue types and found that cell density was highest in glioblastoma, intermediate in WHO grade III gliomas and lowest in non-neoplastic cases (Fig. 3F). The cell density in glioblastoma was ~5 fold higher than in WHO grade III gliomas. Our evaluations show that the cellular density of both fresh and frozen tissues can be readily assessed by SRS imaging.

Similar to the artifacts present in frozen samples of non-neoplastic brain, we also noted freezing-related artifacts in the SRS images from frozen brain tumor specimens. To compare these images with those from non-frozen tissue we imaged fresh tissue from a glioma immediately following resection. Figure 4A shows an SRS image of an entire fresh biopsy specimen from an oligodendroglioma (WHO grade II) (case 44, specimen BL5E-1). The extent of cellularity was heterogeneous across the tissue with some areas containing tumor cells infiltrating into the non-neoplastic brain adjacent to the main tumor mass (Fig. 4A and B, yellow squares) and other areas comprised of densely cellular tumor with higher cellularity (Fig. 4A and C, magenta squares). Notably, the quality of the SRS imaging from fresh tissue was superior to that of frozen tissue with improved visualization of cell nuclei and its morphology in particular. Since SRS imaging does not require sectioning, the tissue does not need to be frozen (Fig. 3 versus Fig. 4), which is an advantage to avoid the above mentioned imaging artifacts.

Evaluation of vascular proliferation

Blood vessels are primarily comprised of endothelial cells, smooth muscle cells and extracellular matrix materials that are all characterized by a relatively high ratio of proteins to lipids (40). Consistent with this profile, in SRS images, blood vessels (capillaries, arteries, or veins) displayed strong protein signals (blue) (Fig. 5A, marked by V, specimen 03#2, case 46). Notably, we readily identified the nuclei of endothelial cells of the capillaries (Fig. 5A, yellow arrowheads) at submicron spatial resolution. The ability to image blood vessels in fresh tissue resections or *in vivo* may be useful for investigating the blood-brain barrier and drug delivery. In our SRS imaging, red blood cells were imaged with the non-Raman frequency at 2800 cm^{-1} in a magenta channel (Fig. 5A, white arrowheads). The red blood cells were readily observed co-distributed within blood vessels. Interestingly, single round doughnut shaped red blood cells were seen in fresh tissue SRS imaging, while in frozen

tissue sections, the red blood cells were often distorted and only aggregates of cells were detected (Fig. 2A).

A hallmark of glioblastoma is the presence of tortuous and thickened blood vessels termed microvascular proliferation (41). In Fig. 5B we show paired SRS and H&E images acquired from a frozen section of a glioblastoma specimen (specimen #2, case 22). In both images the distribution of blood vessels is identical. Moreover, the branched structures of the proliferated vasculature are readily observed. Microvascular proliferation is particularly distinct in the SRS images due to the sharp contrast between the blue vasculature and the green lipids (marked by V, Fig. 5C). Because of the quantitative nature of SRS imaging, it offers the significant advantage of being able to quantify the extent of vascular proliferation in brain tumors.

Discrimination of necrosis and viable tumor

Another diagnostic hallmark of glioblastoma is necrosis. These regions develop due to multiple factors within the tumor and its microenvironment including the induction of clotting cascades that result in thrombosis within the microvasculature of gliomas (42), apoptosis of endothelial cells, angiogenesis which can result in aberrant vessel formation (43) and also to dynamic microenvironmental and tumor cell intrinsic factors that can trigger tumor cell apoptosis (44,45). Areas of necrosis can also result following treatment. In some glioblastoma cases, tumor cells accumulate around the regions of necrosis in what is called “pseudopalisading” necrosis (46). In one of our glioblastoma cases (case 9), we found extensive necrosis accompanying viable tumor (Fig. 6). The tumor had been biopsied two weeks prior to the resection of the large “butterfly” lesion that traversed the anterior corpus callosum. In these untreated resection specimens (i.e. no chemotherapy and no radiation therapy) we found extensive necrosis accompanying viable tumor, a hallmark of GBM (Fig. 6). In SRS imaging, necrotic tissue featured a markedly disordered distribution and aggregation of both proteins and lipids. These necrotic regions (Fig. 6, marked “N”) were completely devoid of viable cell nuclei. By comparing different biopsy specimens from this case (Fig. 6A, C and E), we found that the protein/lipid ratio varied widely between the specimens. Generally, however, regions of tissue comprised of viable and high concentration of tumor cells (Fig. 6, marked “T”) as well as blood vessels with microvascular proliferation (Fig. 6, marked “V”) displayed stronger protein signals (blue) than the protein signals observed in necrotic zones. Coupled with the complete absence of nuclei in the necrotic regions, the boundary between necrosis and viable tumor was clearly identified with sub-cellular resolution (Fig. 6B, D, and F). SRS imaging could also identify regions of necrosis following treatment of the tumor in a case of recurrent anaplastic oligodendroglioma case (WHO III, case 15, specimen K11).

The spatial distribution of necrotic tissue and viable tumor could be very complex. For example, Fig. 6A shows separate regions of necrosis and viable tumor; Fig. 6C shows a small tumor core surrounded by necrotic tissue; and Fig. 6E shows a mixed distribution of necrosis and viable tumor. Our results confirm that SRS imaging could rapidly discriminate necrosis from viable tumor based solely on tissue and cellular morphology, without the need for statistical analysis or computer/mathematical algorithms and signatures. In future work,

registration of tumor biopsies to the site of removal relative to pre-operative magnetic resonance images via neuronavigation methods would allow us to delineate three-dimensional maps of normal tissue/necrosis/tumor distributions and margins with higher spatial resolution (Supplementary Fig. S1A and B).

Label-free imaging of collagen

Finally, in two fresh tissue specimens from a recurrent glioblastoma, SRS imaging revealed extensive fibrillar collagen deposition in the extracellular matrix (Fig. 7A and C, case 52). Seventeen months earlier this patient had a resection performed at an outside hospital of a large right-sided fronto-temporal lesion. On histology, that tumor demonstrated all the classic histologic features of a glioblastoma. The recurrent tumor, however, had the striking features of a gliosarcoma, a morphological variant of glioblastoma in which the malignant cells display a biphasic pattern of differentiation comprised of both glial and mesenchymal components. As a result of the mesenchymal differentiation, these tumors often have extensive collagen deposition. On SRS images of the fresh (unfrozen) tissue, the distribution, morphology, and orientation of the collagen fiber bundles were clearly visualized based on very strong protein signal (blue fibers in Fig. 7B and D). In some regions the cancer cells displayed oval nuclei while in the regions of intersecting dense collagen bundles, the nuclei of the tumor cells were elongated and spindle shaped (e.g., Fig. 7B, white arrowheads). The unique ability of SRS microscopy to visualize the relationship between tumor cells and the extracellular matrix components may provide new insights into tumor stromal interaction in the pathogenesis of brain tumors. Although second harmonic generation (SHG) is the optimal method to image collagen with high specificity, SRS imaging is unique since it offers a relatively simple approach for simultaneously imaging cellular proteins, lipids, blood, and components of the extracellular matrix with accuracy and all assessed by tracking only two Raman shifts.

Discussion

We present a comprehensive direct comparison and evaluation of SRS imaging and H&E staining. Based on our analysis, we show that we can use SRS imaging to readily detect many diagnostic hallmarks that are essential for brain tumor identification and classification. We find that SRS imaging offers similar information as that provided by the review of H&E stained frozen sections with large-scale data. Cell nuclei and cell density are well visualized and cell density can be quantified. Moreover, because of the sharp contrast between lipids and proteins that SRS imaging provides, vascular proliferation, red blood cells, and necrosis can be easily discriminated by SRS techniques. Of particular interest, the high quality of the SRS images of fresh brain tumor resection tissue permits the visualization of structures that are not detectable using standard H&E approaches, which require freezing of the specimen (Supplementary Table S2).

Notably, we were able to visualize small bulbous protrusions dotting the surface of myelinated fibers in white matter areas that have been infiltrated by oligodendroglioma cells (Fig. 4, case 44). This alternation was not present in normal white matter areas, suggesting that the infiltrating oligodendroglioma cells may perturb and alter myelin structure. It has

long been appreciated that glioma cells, particularly those of oligodendroglioma, aggregate around neuronal perikaryons, a histologic feature known as perineuronal satellitosis (39). The interaction of glioma cells with neurons has recently been shown to provide an adaptive growth advantage to the tumor cells with active neurons promoting the proliferation of glioma cells via the secretion of the synaptic protein neuroligin-3 (NLGN3) (47,48). Our unexpected observation of a marked alternation of myelinated fibers in our SRS images of oligodendroglioma suggests a potentially new way in which oligodendroglioma cells may sculpt their microenvironment, one that could potentially provide an adaptive advantage.

In addition, SRS imaging of fresh gliosarcoma tissue also allowed us to detect abundant intracellular lipid droplets within the glioma cells, another feature that is not detectable by standard H&E stained sections (Fig. 7B and D, case 52). Recent work has shown that glioma cells in tissue culture adapt to stressors such as nutrient deprivation and hypoxia by generating lipid droplets (49,50). In those studies, glioma cell survival following nutrient deprivation was attenuated by suppressing lipid droplet biogenesis by either chemical or genetic interventions. The significance of the lipid droplets detected in our work is unclear, but the ability to readily detect them using SRS imaging suggests that this is a powerful methodology for investigating the importance of lipid biology in human tumors. Further studies will be needed to evaluate and quantify the diagnostic value of characterizing bulbous protrusions in myelinated fibers, lipid droplet formation, collagen deposition and other features that have been underappreciated due to the lack of their visualization with H&E staining.

In summary, label-free SRS imaging of human brain tumor tissue provides pathology-like information with evident molecular contrasts and high-level sensitivity. This approach could allow for rapid intraoperative brain tumor diagnosis based on detailed histology images, while avoiding freezing, sectioning and staining of the tissue, thereby eliminating tissue-processing artifacts. SRS imaging also offers insights into new diagnostic features beyond those revealed by H&E staining. Our SRS imaging work provides significant progress toward the longer-term goal of deploying this promising tool for use in surgical decision-making workflows and of fostering its widespread adoption by medical teams (Fig. S1B). The accompanying dataset (doi:10.7910/DVN/EZW4EK; Supplementary Materials) is made available to help drive growth of this emerging area.

Supplementary Material

Refer to Web version on PubMed Central for supplementary material.

Acknowledgements

We would like to thank Patricia Purcell for critical reading and editing of the manuscript, Armen Changelian for assistance with reagents, Ang Li for technical support on the lasers, and Revaz Machaidze for help collect fresh tissue.

Financial support: This work was funded by Harvard Catalyst | The Harvard Clinical and Translational Science Center (National Center for Research Resources and the National Center for Advancing Translational Sciences, National Institutes of Health Award UL1 TR001102) and financial contributions from Harvard University and its affiliated academic healthcare centers (A.J.G., X.S.X., N.Y.A.), National Institute of Health (NIH) Director's New

Innovator Award (1DP2OD007383-01 to N.Y.A.), the National Center for Image Guided Therapy grant P41RR019703 (A.J.G., N.Y.A.), and NIH Pathway to Independence K99/R00 Award (1K99EB020749-1 to F.L.).

References

1. McGirt MJ, Chaichana KL, Gathinji M, Attenello FJ, Than K, Olivi A, et al. Independent association of extent of resection with survival in patients with malignant brain astrocytoma. J Neurosurg. 2009; 110(1):156–62. [PubMed: 18847342]
2. Asthagiri AR, Pouratian N, Sherman J, Ahmed G, Shaffrey ME. Advances in brain tumor surgery. Neurol Clin. 2007; 25(4):975–1003, viii-ix. [PubMed: 17964023]
3. Ulmer S. Intraoperative perfusion magnetic resonance imaging: Cutting-edge improvement in neurosurgical procedures. World J Radiol. 2014; 6(8):538–43. [PubMed: 25170392]
4. Pallud J, Varlet P, Devaux B, Geha S, Badoual M, Deroulers C, et al. Diffuse low-grade oligodendrogliomas extend beyond MRI-defined abnormalities. Neurology. 2010; 74(21):1724–31. [PubMed: 20498440]
5. Kiernan, JA. Histological and histochemical methods : theory and practice. Scion; Oxford: 2008.
6. Chen B, Wang H, Ge P, Zhao J, Li W, Gu H, et al. Gross total resection of glioma with the intraoperative fluorescence-guidance of fluorescein sodium. Int J Med Sci. 2012; 9(8):708–14. [PubMed: 23091408]
7. Golby, AJ. Image-guided neurosurgery. Academic Press is an imprint of Elsevier; Amsterdam: 2015.
8. Li Y, Rey-Dios R, Roberts DW, Valdes PA, Cohen-Gadol AA. Intraoperative fluorescence-guided resection of high-grade gliomas: a comparison of the present techniques and evolution of future strategies. World Neurosurg. 2014; 82(1-2):175–85. [PubMed: 23851210]
9. Skirboll SS, Ojemann GA, Berger MS, Lettich E, Winn HR. Functional cortex and subcortical white matter located within gliomas. Neurosurgery. 1996; 38(4):678–84. [PubMed: 8692384]
10. Krafft C, Sobottka SB, Schackert G, Salzer R. Near infrared Raman spectroscopic mapping of native brain tissue and intracranial tumors. Analyst. 2005; 130(7):1070–7. [PubMed: 15965532]
11. Kalkanis SN, Kast RE, Rosenblum ML, Mikkelsen T, Yurgelevic SM, Nelson KM, et al. Raman spectroscopy to distinguish grey matter, necrosis, and glioblastoma multiforme in frozen tissue sections. J Neurooncol. 2014; 116(3):477–85. [PubMed: 24390405]
12. Jermyn M, Mok K, Mercier J, Desroches J, Pichette J, Saint-Arnaud K, et al. Intraoperative brain cancer detection with Raman spectroscopy in humans. Sci Transl Med. 2015; 7(274):274ra19.
13. Kut C, Chaichana KL, Xi JF, Raza SM, Ye XB, McVeigh ER, et al. Detection of human brain cancer infiltration ex vivo and in vivo using quantitative optical coherence tomography. Sci Transl Med. 2015; 7(292)
14. Bohringer HJ, Lankenau E, Stellmacher F, Reusche E, Huttmann G, Giese A. Imaging of human brain tumor tissue by near-infrared laser coherence tomography. Acta Neurochir (Wien). 2009; 151(5):507–17. [PubMed: 19343270]
15. Woodbury EJ, Ng WK. Ruby operation in the near IR. Proc Inst Radio Eng. 1962; 50:2367.
16. Owyoung A, Jones ED. Stimulated Raman spectroscopy using low-power cw lasers. Opt Lett. 1977; 1(5):152–54. [PubMed: 19680362]
17. Ploetz E, Laimgruber S, Berner S, Zinth W, Gilch P. Femtosecond stimulated Raman microscopy. Appl Phys B. 2007; 87(3):389–93.
18. Freudiger CW, Min W, Saar BG, Lu S, Holtom GR, He C, et al. Label-free biomedical imaging with high sensitivity by stimulated Raman scattering microscopy. Science. 2008; 322(5909):1857–61. [PubMed: 19095943]
19. Ozeki Y, Dake F, Kajiyama S, Fukui K, Itoh K. Analysis and experimental assessment of the sensitivity of stimulated Raman scattering microscopy. Opt Express. 2009; 17(5):3651–8. [PubMed: 19259205]
20. Nandakumar P, Kovalev A, Volkmer A. Vibrational imaging based on stimulated Raman scattering microscopy. New J Phys. 2009:11.
21. Zhang D, Sipchenko MN, Cheng JX. Highly Sensitive Vibrational Imaging by Femtosecond Pulse Stimulated Raman Loss. J Phys Chem Lett. 2011; 2(11):1248–53. [PubMed: 21731798]

22. Ozeki Y, Umemura W, Otsuka Y, Satoh S, Hashimoto H, Sumimura K, et al. High-speed molecular spectral imaging of tissue with stimulated Raman scattering. Nature Photon. 2012; 6(12):844–50.
23. Wang P, Li J, Wang P, Hu CR, Zhang D, Sturek M, et al. Label-free quantitative imaging of cholesterol in intact tissues by hyperspectral stimulated Raman scattering microscopy. Angew Chem Int Ed. 2013; 52(49):13042–6.
24. Camp CH Jr. Lee YJ, Heddleston JM, Hartshorn CM, Hight Walker AR, Rich JN, et al. High-Speed Coherent Raman Fingerprint Imaging of Biological Tissues. Nature Photon. 2014; 8:627–34.
25. Lu FK, Basu S, Igras V, Hoang MP, Ji MB, Fu D, et al. Label-free DNA imaging in vivo with stimulated Raman scattering microscopy. Proc Natl Acad Sci U S A. 2015; 112(37):11624–29. [PubMed: 26324899]
26. Cheng JX, Xie XS. Vibrational spectroscopic imaging of living systems: An emerging platform for biology and medicine. Science. 2015; 350(6264):aaa8870. [PubMed: 26612955]
27. Drutis DM, Hancewicz TM, Pashkovski E, Feng L, Mihalov D, Holtom G, et al. Three-dimensional chemical imaging of skin using stimulated Raman scattering microscopy. J Biomed Opt. 2014; 19(11):111604. [PubMed: 24858033]
28. Cheng, J-X.; Xie, XS. Coherent Raman scattering microscopy. CRC Press; Boca Raton, FL: 2013.
29. Evans CL, Xu X, Kesari S, Xie XS, Wong ST, Young GS. Chemically-selective imaging of brain structures with CARS microscopy. Opt Express. 2007; 15(19):12076–87. [PubMed: 19547572]
30. Uckermann O, Galli R, Tamosaityte S, Leipnitz E, Geiger KD, Schackert G, et al. Label-free delineation of brain tumors by coherent anti-Stokes Raman scattering microscopy in an orthotopic mouse model and human glioblastoma. PLoS One. 2014; 9(9):e107115. [PubMed: 25198698]
31. Ji M, Orringer DA, Freudiger CW, Ramkissoon S, Liu X, Lau D, et al. Rapid, label-free detection of brain tumors with stimulated Raman scattering microscopy. Sci Transl Med. 2013; 5(201): 201ra119.
32. Ji M, Lewis S, Camelo-Piragua S, Ramkissoon SH, Snuderl M, Venneti S, et al. Detection of human brain tumor infiltration with quantitative stimulated Raman scattering microscopy. Sci Transl Med. 2015; 7(309):309ra163.
33. Freudiger CW, Pfannl R, Orringer DA, Saar BG, Ji MB, Zeng Q, et al. Multicolored stain-free histopathology with coherent Raman imaging. Lab Invest. 2012; 92(10):1492–502. [PubMed: 22906986]
34. Fedorov A, Beichel R, Kalpathy-Cramer J, Finet J, Fillion-Robin JC, Pujol S, et al. 3D Slicer as an image computing platform for the Quantitative Imaging Network. Magn Reson Imaging. 2012; 30(9):1323–41. [PubMed: 22770690]
35. Lu FK, Ji M, Fu D, Ni X, Freudiger CW, Holtom G, et al. Multicolor stimulated Raman scattering (SRS) microscopy. Mol Phys. 2012; 110(15-16):1927–32. [PubMed: 23504195]
36. Fu D, Ye T, Matthews TE, Yurtsever G, Warren WS. Two-color, two-photon, and excited-state absorption microscopy. J Biomed Opt. 2007; 12(5):054004. [PubMed: 17994892]
37. Schain AJ, Hill RA, Grutzendler J. Label-free in vivo imaging of myelinated axons in health and disease with spectral confocal reflectance microscopy. Nat Med. 2014; 20(4):443–9. [PubMed: 24681598]
38. Nave KA. Myelination and support of axonal integrity by glia. Nature. 2010; 468(7321):244–52. [PubMed: 21068833]
39. Louis DN, Ohgaki H, Wiestler OD, Cavenee WK, Burger PC, Jouvet A, et al. The 2007 WHO classification of tumours of the central nervous system. Acta Neuropathol. 2007; 114(2):97–109. [PubMed: 17618441]
40. Baluk P, Hashizume H, McDonald DM. Cellular abnormalities of blood vessels as targets in cancer. Curr Opin Genet Dev. 2005; 15(1):102–11. [PubMed: 15661540]
41. Brem S. The role of vascular proliferation in the growth of brain tumors. Clin Neurosurg. 1976; 23:440–53. [PubMed: 975695]
42. Zerrouqi A, Pyrzynska B, Brat DJ, Van Meir EG. P14ARF suppresses tumor-induced thrombosis by regulating the tissue factor pathway. Cancer Res. 2014; 74(5):1371–8. [PubMed: 24398474]

43. Rong Y, Durden DL, Van Meir EG, Brat DJ. 'Pseudopalisading' necrosis in glioblastoma: a familiar morphologic feature that links vascular pathology, hypoxia, and angiogenesis. J Neuropathol Exp Neurol. 2006; 65(6):529–39. [PubMed: 16783163]
44. Kim D, Fiske BP, Birsoy K, Freinkman E, Kami K, Possemato RL, et al. SHMT2 drives glioma cell survival in ischaemia but imposes a dependence on glycine clearance. Nature. 2015; 520(7547):363–7. [PubMed: 25855294]
45. Aldape K, Zadeh G, Mansouri S, Reifenberger G, von Deimling A. Glioblastoma: pathology, molecular mechanisms and markers. Acta Neuropathol. 2015; 129(6):829–48. [PubMed: 25943888]
46. Wippold FJ 2nd, Lammle M, Anatelli F, Lennerz J, Perry A. Neuropathology for the neuroradiologist: palisades and pseudopalisades. AJNR Am J Neuroradiol. 2006; 27(10):2037–41. [PubMed: 17110662]
47. Venkatesh HS, Johung TB, Caretti V, Noll A, Tang Y, Nagaraja S, et al. Neuronal Activity Promotes Glioma Growth through Neuroligin-3 Secretion. Cell. 2015; 161(4):803–16. [PubMed: 25913192]
48. Filbin MG, Segal RA. How neuronal activity regulates glioma cell proliferation. Neuro Oncol. 2015; 17(12):1543–4. [PubMed: 26359210]
49. Cabodevilla AG, Sanchez-Caballero L, Nintou E, Boiadjieva VG, Picatoste F, Gubern A, et al. Cell survival during complete nutrient deprivation depends on lipid droplet-fueled beta-oxidation of fatty acids. J Biol Chem. 2013; 288(39):27777–88. [PubMed: 23940052]
50. Bensaad K, Favaro E, Lewis CA, Peck B, Lord S, Collins JM, et al. Fatty acid uptake and lipid storage induced by HIF-1alpha contribute to cell growth and survival after hypoxiareoxygenation. Cell Rep. 2014; 9(1):349–65. [PubMed: 25263561]

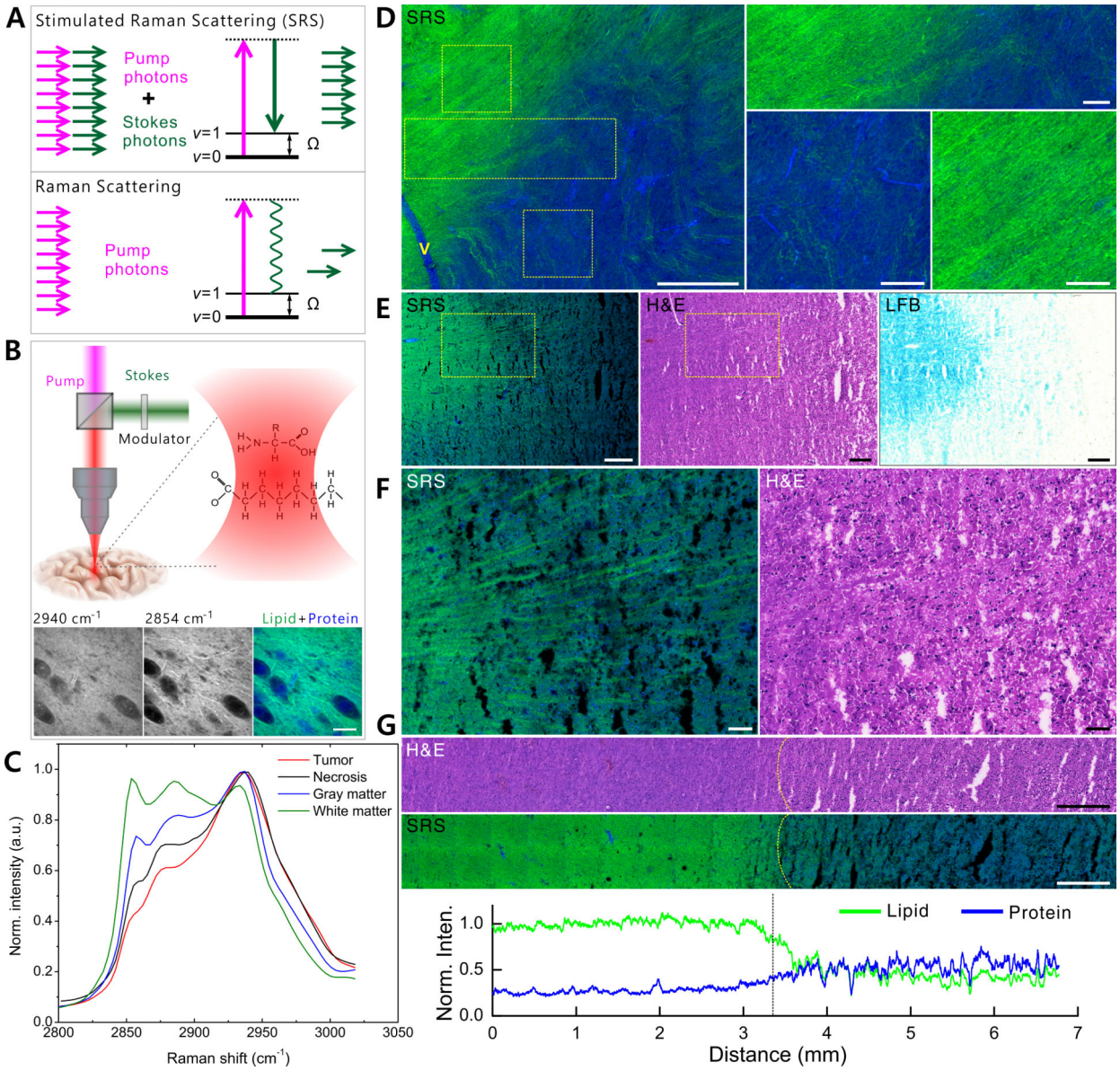

Fig. 1. Label-free chemical imaging of human brain with stimulated Raman scattering (SRS) microscopy

(A) Energy diagrams of stimulated Raman scattering (SRS) and spontaneous Raman scattering. In spontaneous Raman scattering, a small amount of photons are shifted in energy from the laser frequency due to their interaction with the vibrational levels of molecules in the sample. The energy shift is defined as Raman shift, which is often reported in wavenumbers (cm^{-1}). Note that spontaneous Raman scattering is typically very weak. SRS occurs when the sample is excited by synchronized pump and Stokes beams of ultrafast lasers. The frequency difference of the two laser beams defines the Raman shift used for imaging. SRS signals are much stronger than spontaneous Raman scattering due to the stimulated emission process. (B) Schematic representation of SRS microscopy (upper), and representative two-color SRS imaging of fresh brain tissue at 2940 and 2854 cm^{-1} (below). (C) SRS spectra of brain tumor, white matter, gray matter, and necrotic tissue show distinct

spectral features. (D) SRS imaging of a fresh human brain tissue sample at the white matter and gray matter junction (green, lipid; blue, protein). White matter is featured by strong lipid signals mainly from the myelin sheath. Gray matter contains lower lipid composition, showing in dark blue. Scale bar, 100 μm. (E) SRS imaging (left) of frozen normal human brain tissue sections from an autopsy case (case A1). SRS imaging could rapidly and clearly identify white and gray matter based on the lipid/protein contrast. In contrast, H&E staining images (middle) did not provide a clear distinction between white and gray matter. White matter was confirmed by LFB staining (right). (F) Zoom-in images in (E) show very fine structures of single myelin fibers at the transition area from white matter to gray matter. (G) A large-scale image of white/gray matter (~7 mm in length) and the intensity profile (sum along the vertical direction) shows that lipid content in the white matter is higher than that of the gray matter by ~2 fold. Scale bars: (D and F), 100 μm; (E and G), 500 μm.

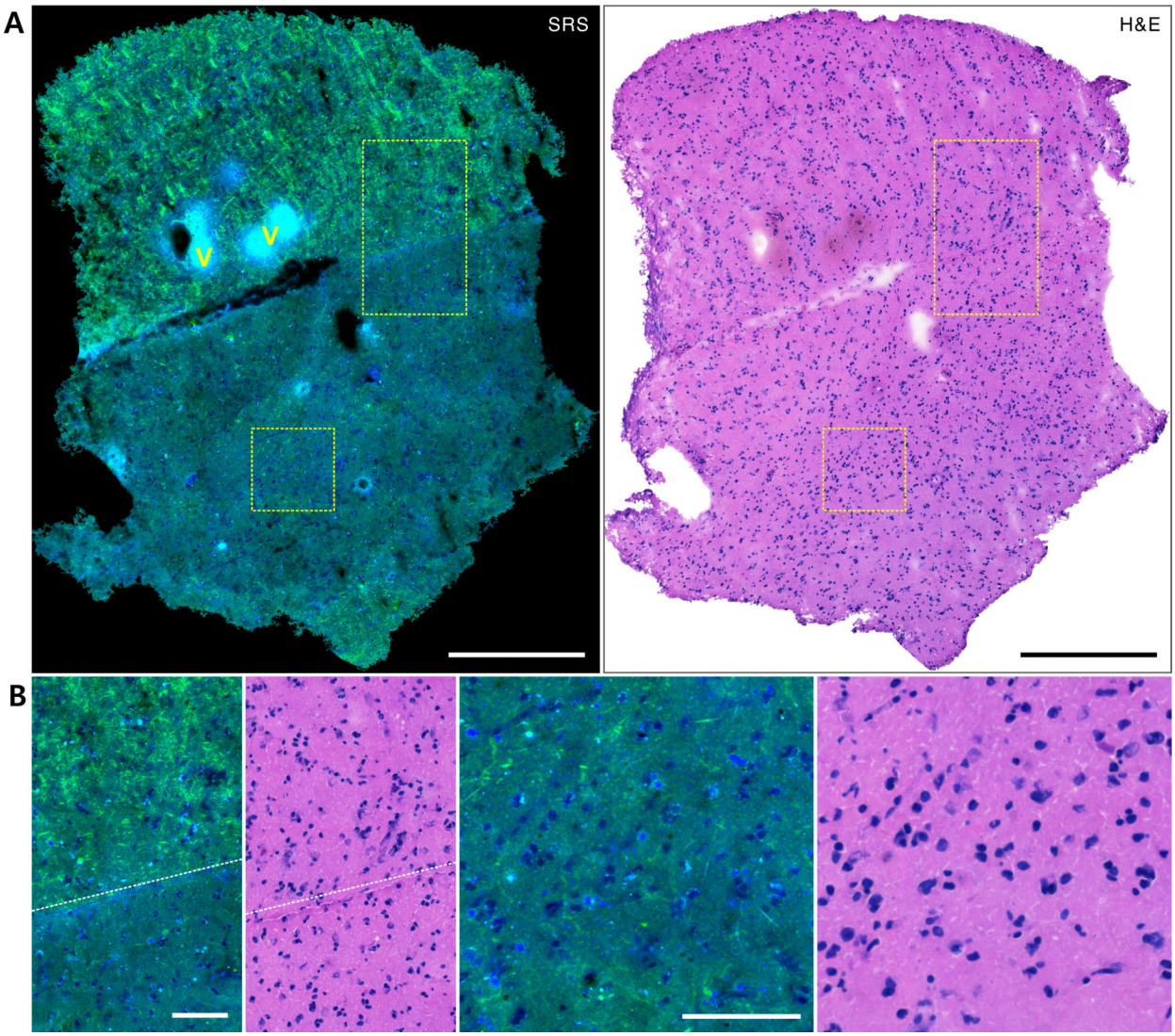

Fig. 2. Paired SRS and H&E imaging of a frozen sectioned whole specimen with cancer cell infiltration

(A) The upper part of the specimen is basically white matter as shown by the strong lipid signals and the condensed myelin fibers, and the bottom part is gray matter with lower lipid signals. Red blood cells are shown in cyan color (marked by V). (B) Zoom-in images display clear white/gray matter margin (left) and single cell nuclei morphology, showing correlation between SRS and H&E (right). The presence of infiltrative cancer cells is confirmed by H&E stained image. Images were from frozen specimen B2 of case 15 (anaplastic oligodendroglioma, grade III). Scale bars: A, 500 μm; B, 100 μm.

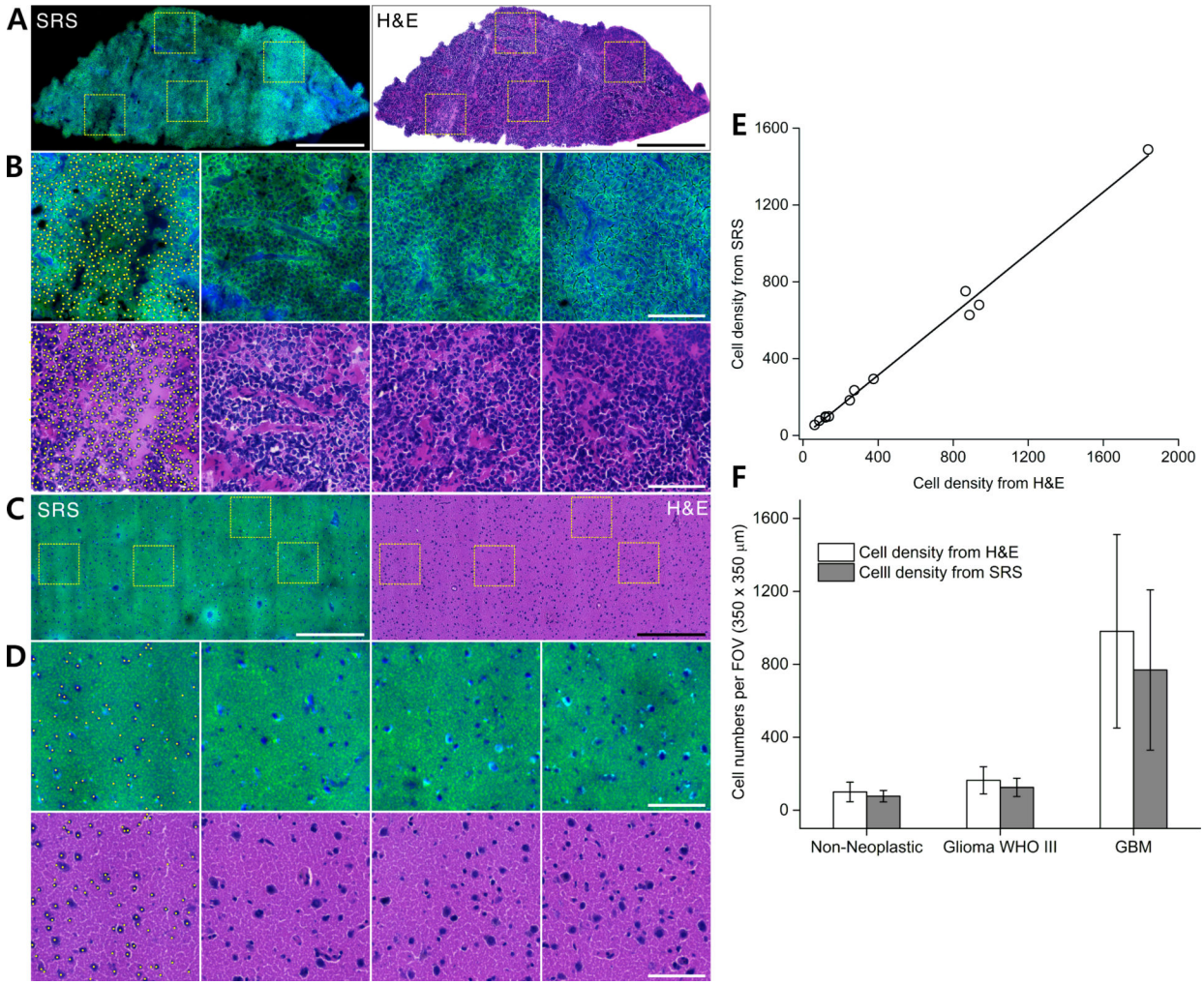

Fig. 3. Quantification of cellularity with paired SRS and H&E imaging of frozen sectioned brain tissue

(A) SRS (left) and H&E stained (right) images of a whole specimen from a GBM case show hypercellularity. (B) Four zoom-in images in (A) demonstrate that the round-shape of the cell nuclei can be clearly visualized. (C) SRS (left) and H&E stained (right) images of a nonneoplastic tissue section show very low cell density (epilepsy). (D) Zoom-in images in (C) show clear single cell nuclei, and correlation between SRS and H&E images. Yellow dots in the zoom-in images demonstrate the cell counting procedure. Images in (A and B) were from frozen specimen #3 of case 22 (GBM) and images in (C and D) were from frozen specimen A1 of case 42 (epilepsy). Scale bar: (A, C), 500 µm; (B, D), 50 µm. (E) Linear correlation plot of cell counting from SRS and H&E images (correlation factor $R^2 = 0.99$). (F) Cell density tracing for non-neoplastic, glioma grade III, and GBM specimens. Data for non-neoplastic tissue include 41 (FOV) from the epilepsy case (case 42) and 69 FOV from the autopsy normal case A1. Data for glioma grade III include 15 FOV from case 39 and 27 FOV from case 15. Data for GBM include 29 FOV from case 22 and 6 FOV from case 9.

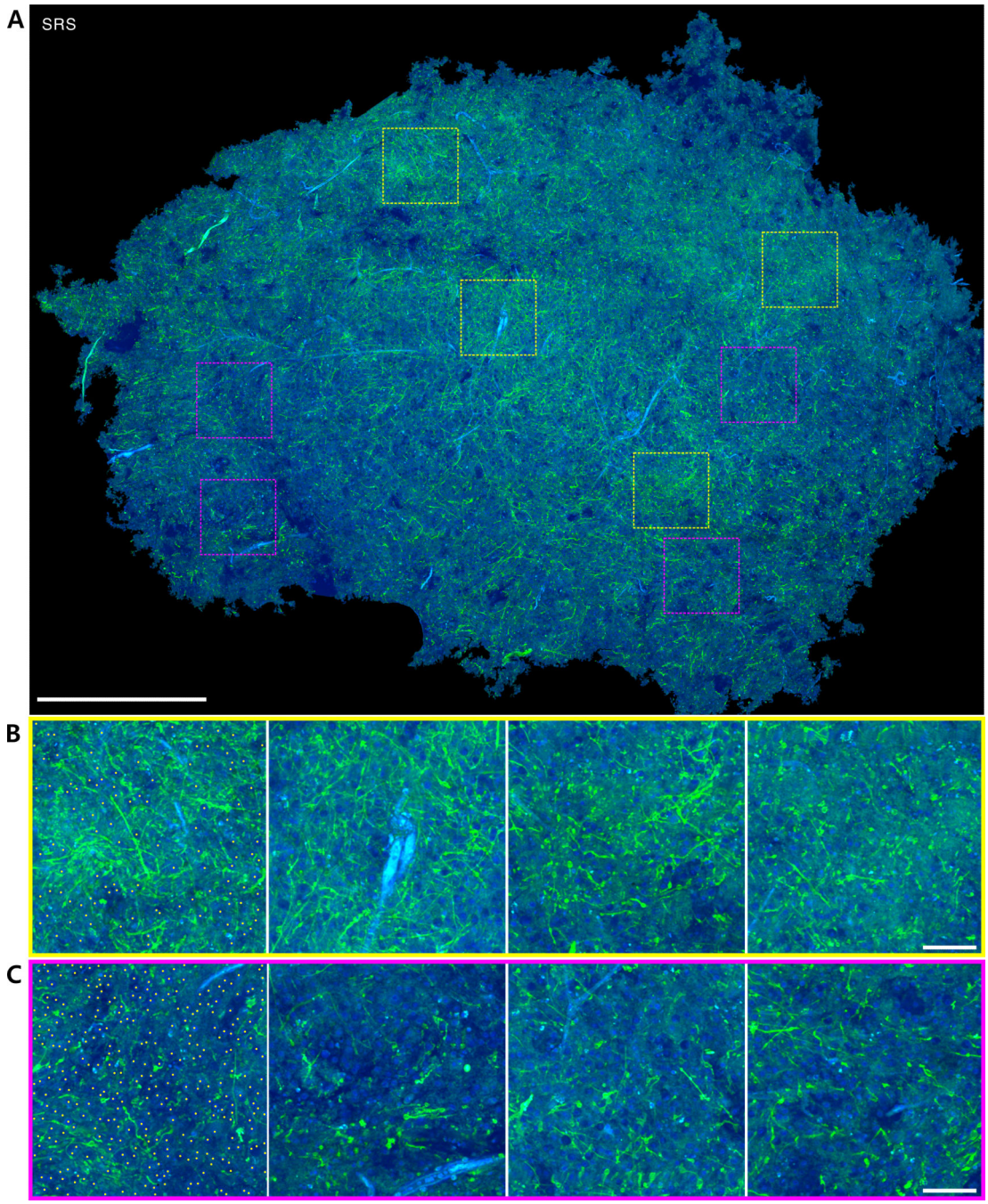

Fig. 4. SRS imaging of fresh human brain tumor tissue

(A) SRS image of the whole fresh specimen (~1 mm in thickness). (B) Four zoom-in images in (A) (yellow squares) show lower cell density, while the other four zoom-in images in (A) (magenta squares) show higher cell density (C), demonstrating tumor heterogeneity. Blood vessels with red blood cells are shown in cyan color. Single myelin fibers were visualized based on the strong lipid contrast with high sensitivity. Images were from fresh specimen BL5E-1 of case 44 (oligodendroglioma grade II). Scale bars: (A), 1 mm; (B, C), 100 μm.

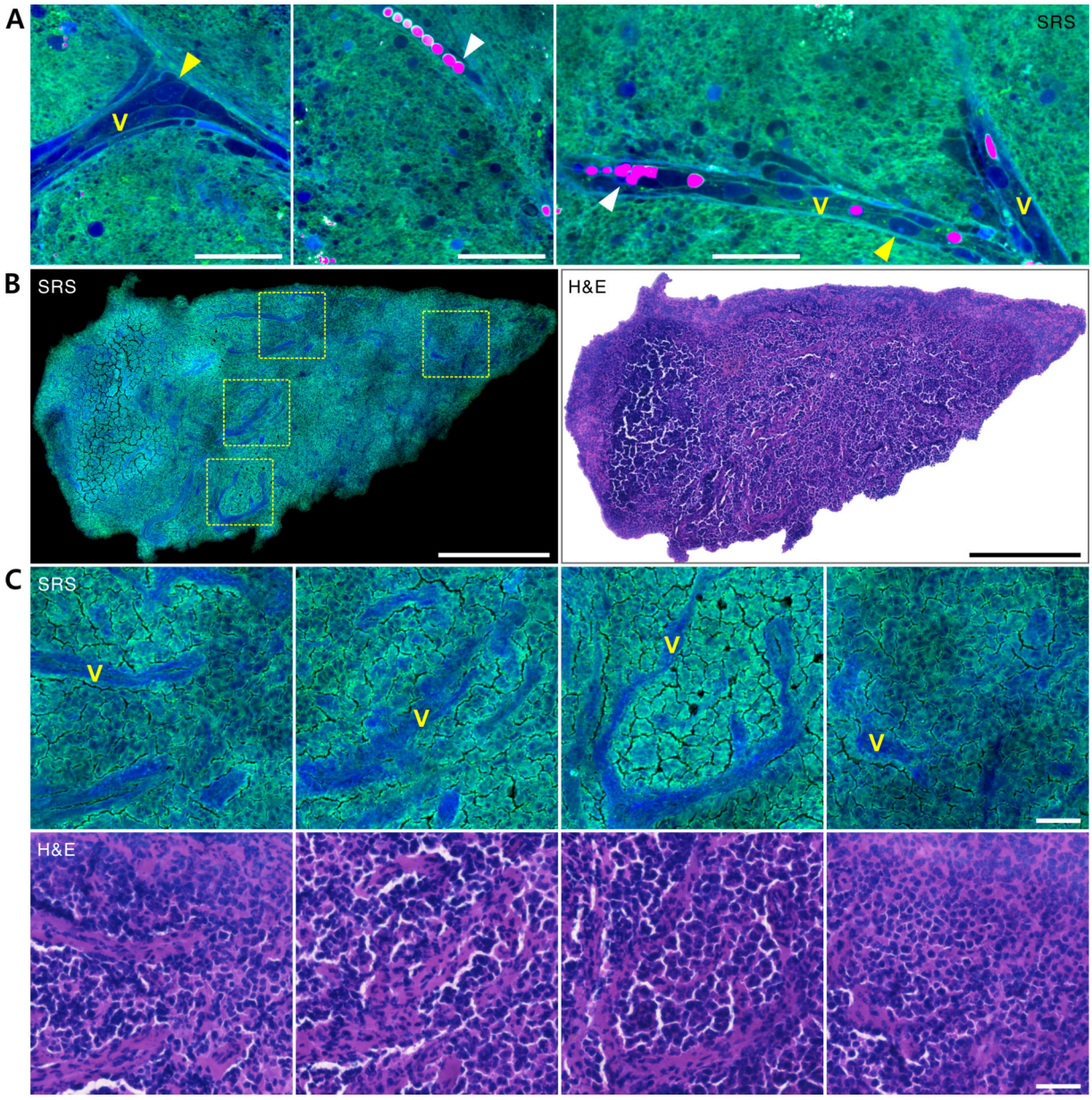

Fig. 5. SRS and H&E stained imaging of blood vessels to characterize vascular proliferation in GBM

(A) SRS imaging of fresh brain tumor tissue shows blood vessels in blue with red blood cells (magenta). Cell nuclei of the endothelial cells of the blood vessels are clearly visualized based on the protein contrast. (B) Paired SRS and H&E imaging of the whole tissue section show vascular proliferation in a GBM case. (C) Zoom-in images of (B) show that the blood vessels can be visualized with high specificity by SRS imaging (marked by V). Images (A) were from fresh specimen 03#2 of case 46 (GBM), images (B and C) were from frozen specimen #2, case 22 (GBM). Scale bars: (A, C), 100 μm; (B), 500 μm.

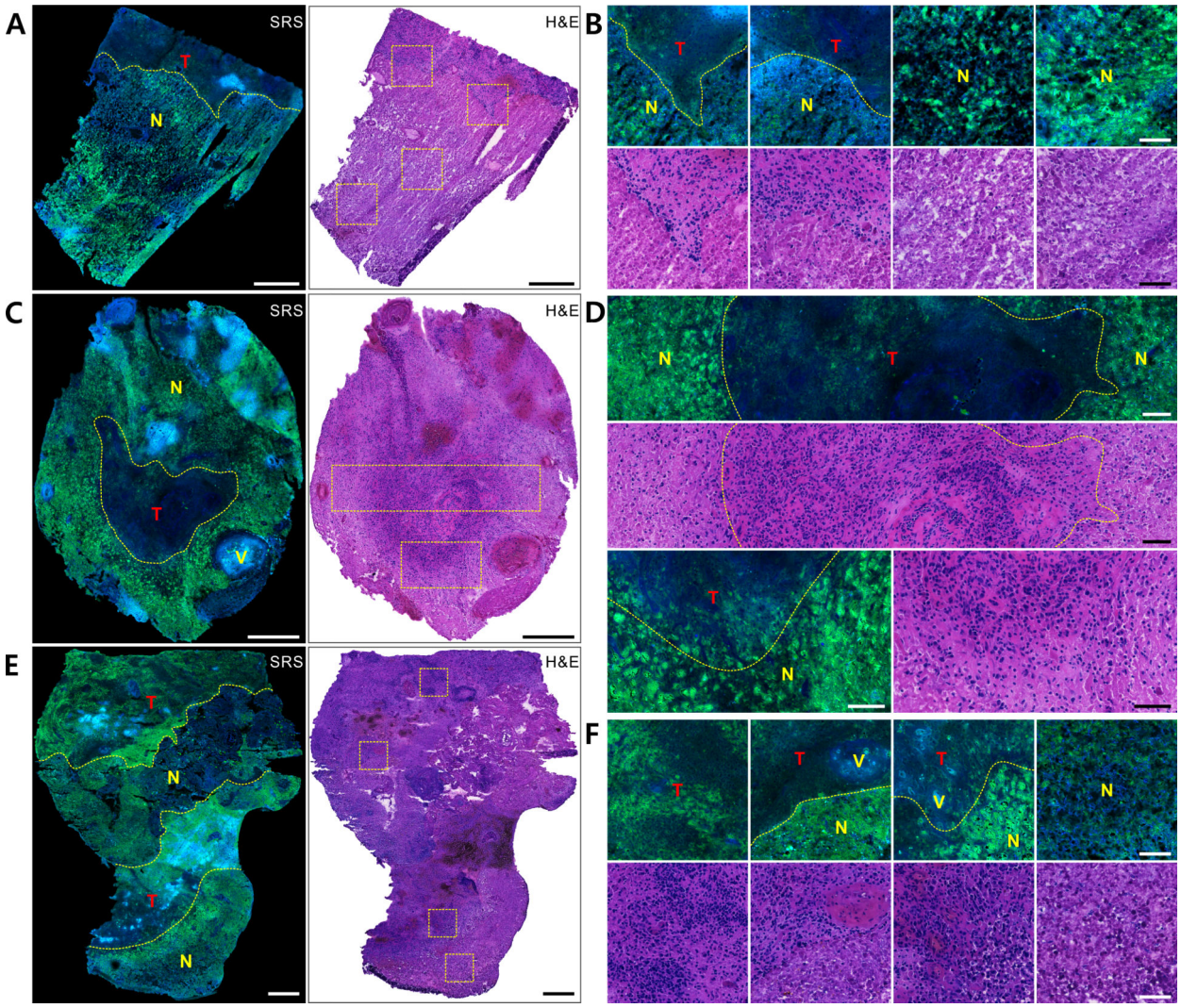

Fig. 6. Paired SRS and H&E stained imaging of tissue from a GBM case shows extensive necrosis

(A) A specimen with extensive necrosis (below, marked by N) and a smaller area of viable tumor (upper, marked by T). (B) A specimen with a small viable tumor core surrounded by necrotic tissue. (C) A specimen with mixed distribution of viable tumor and necrosis. Zoom-in images in (A, C, E) are shown in (B, D F), respectively. Necrosis and viable tumor show very different morphological features and the boundary between these regions is resolved with sub-cellular resolution. All images were from case 9 (GBM). Scale bars: (A, C, E), 500 μm; (B, D, F), 100 μm.

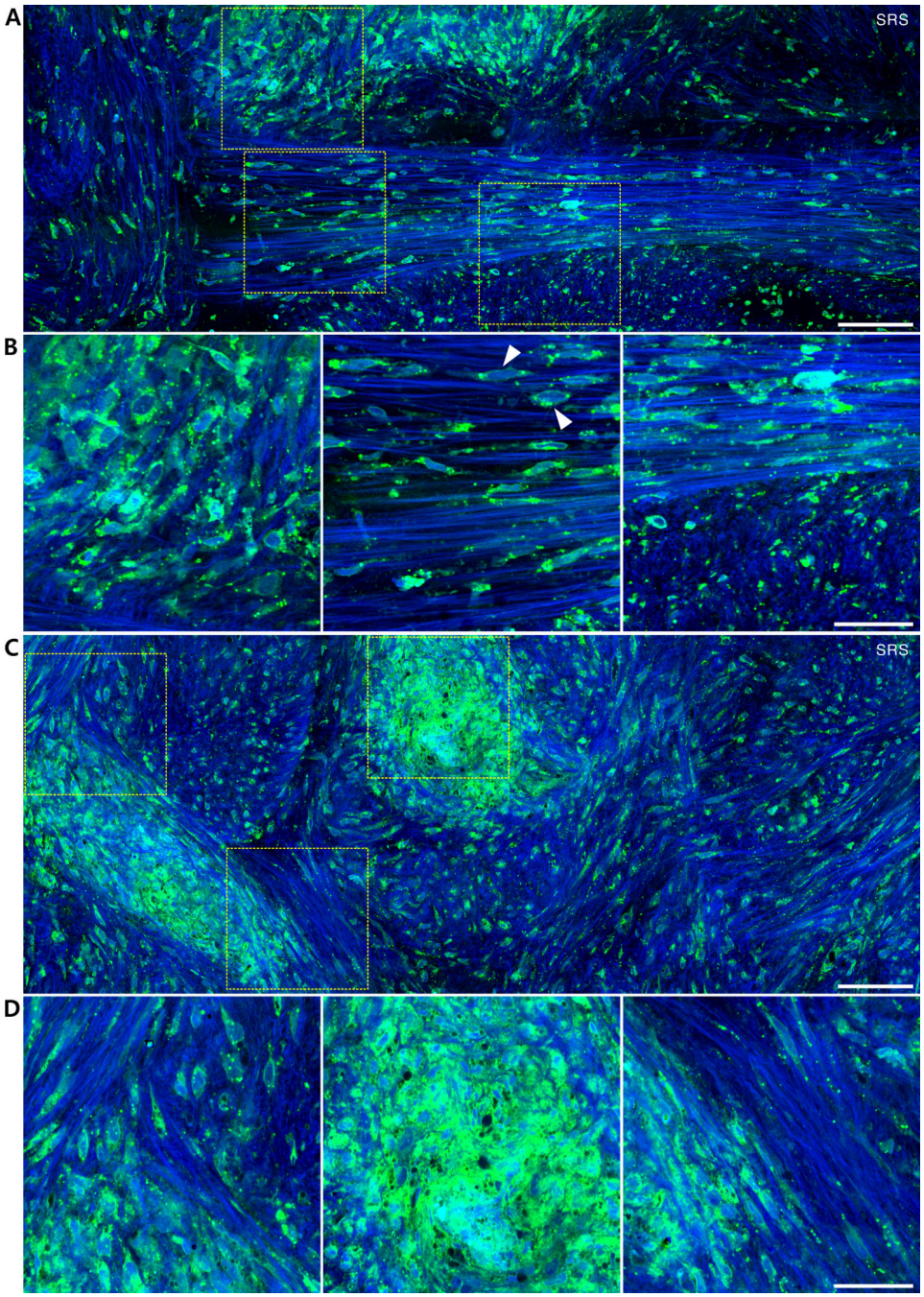

Fig. 7. SRS imaging of massive collagen deposition in a fresh specimen from a recurrent/residual GBM surgical case

(A, C) Two representative large fields of view of the fresh human brain tumor tissue show the co-distribution of collagen and tumor cells. Both isolated single cells and cell clusters are observed. Zoom-in images of (A, C) are shown in (B, D), respectively. A lot of lipid droplets are found in the condensed cells region. Images were from fresh specimens of case 52. Scale bars: (A, C), 100 μm; (B, D), 50 μm.